Allosteric modulation of the SARS-CoV-2 spike conformation

Marco A. Díaz-Salinas[1], Qi Li[2], Monir Ejemel[2], Yang Wang[2], James B. Munro[1,3,*]

[1]Department of Microbiology and Physiological Systems, University of Massachusetts Chan Medical School, Worcester, MA 01605, USA.

[2]MassBiologics of the University of Massachusetts Chan Medical School, Boston, MA 02126, USA.

[3]Department of Biochemistry and Molecular Biotechnology, University of Massachusetts Chan Medical School, Worcester, MA 01605, USA.

*Corresponding author. Email: james.munro@umassmed.edu.

ABSTRACT

Severe acute respiratory syndrome coronavirus 2 (SARS-CoV-2) infects host cells through binding to angiotensin-converting enzyme 2 (ACE2), which is mediated by the receptor-binding domain (RBD) of the viral spike (S) glycoprotein. Structural data and real-time analysis of conformational dynamics have shown that S can adopt multiple conformations, which mediate the exposure of the ACE2-binding site in the RBD. Here, using single-molecule Förster resonance energy transfer (smFRET) imaging we report the effects of ACE2 and antibody binding on the conformational dynamics of S from the Wuhan-1 strain and the B.1 variant (D614G). We found that antibodies that target diverse epitopes, including those distal to the RBD, stabilize the RBD in a position competent for ACE2 binding. Parallel solution-based binding experiments using fluorescence correlation spectroscopy (FCS) indicated antibody-mediated enhancement of ACE2 binding. These findings inform on novel strategies for therapeutic antibody cocktails.

INTRODUCTION

Emerging severe acute respiratory syndrome coronavirus 2 (SARS-CoV-2) is the etiologic agent of the coronavirus disease 2019 (COVID-19) pandemic(*1*). Despite the existence of efficacious COVID-19 vaccines(*2*), urgent needs remain for therapeutic strategies and innovative vaccines to control this unprecedented situation, as well as to stop the emergence of new variants of concern(*3*).

To infect host cells, SARS-CoV-2 binds the cell receptor angiotensin-converting enzyme 2 (ACE2) through its envelope glycoprotein spike (S), which subsequently promotes membrane fusion and cell entry(*1*, *4–11*). S is a trimer of heterodimers, with each protomer consisting of S1 and S2 subunits (Fig. 1). S1 contains the receptor-binding domain (RBD), which includes the ACE2 receptor binding motif (RBM). S2, which forms the spike stalk, undergoes a large-scale refolding during promotion of membrane fusion(*12–15*). Structures of the soluble trimeric ectodomain of the SARS-CoV-2 S glycoprotein in two prefusion conformations have been reported(*10*, *11*, *16*), demonstrating that the RBD of each protomer can independently adopt either a “down” (closed) or an “up” (open) position, giving rise to asymmetric trimer

53 conformations (Fig. 1A). The RBM is occluded in the down conformation, suggesting that RBD
54 transition from the down to the up conformation is required for binding the ACE2 receptor.
55 Indeed, structures of S bound to ACE2 show the RBD in the up conformation(*17*). Structural
56 data were corroborated by real-time analysis of the conformational dynamics of S through
57 smFRET imaging(*18*).

58 These data suggest that modulating the conformational equilibrium of the RBD of S might be a
59 means of controlling SARS-CoV-2 infectivity and neutralization sensitivity. Early in the
60 COVID-19 pandemic, the SARS-CoV-2 S variant D614G (strain B.1) supplanted the ancestral
61 virus (strain Wuhan-1) worldwide, and structural analysis showed that D614G disrupts an
62 interprotomer contact(*19*). This disruption results in a shift in the RBD conformation toward the
63 ACE2 binding-competent state, consistent with increases in *in vitro* virus-cell binding mediated
64 by ACE2 and infectivity(*16*, *20*). At the same time, the enhanced exposure of the receptor-
65 binding site in the D614G variant led to increased sensitivity to neutralizing antibodies(*21*).
66 Furthermore, the RBD showed stabilization in the up position, as well as an intermediate
67 conformation, upon treatment with a neutralizing S2 stalk-directed antibody(*22*, *23*).

68 Here we report on the conformational dynamics of SARS-CoV-2 S in the absence or presence of
69 ligands visualized using an smFRET imaging assay (Fig. 1A). Our results indicate that ACE2
70 binding is controlled by the intrinsic conformational dynamics of the RBD, with ACE2 capturing
71 the intrinsically accessible up conformation rather than inducing a conformational change. We
72 find that antibodies that target diverse epitopes—including epitopes in the NTD and in the S2
73 stalk, which are distal to the RBD—tend to shift the RBD equilibrium on the D614 spike toward
74 the up conformation, enhancing ACE2 binding. The D614G spike existed in an equilibrium
75 where the RBD favors the up conformation prior to antibody binding. Nonetheless, antibodies
76 that target the S2 stalk further promoted the RBD-up conformation on the D614G spike. We thus
77 observe long-range allosteric modulation of the RBD equilibrium, which in turn regulates
78 exposure of the ACE2-binding site. Inducing exposure of key neutralizing epitopes with
79 antibodies will inform the design of novel therapeutic cocktails(*24–26*).

80

81 **RESULTS**

Tagged SARS-CoV-2 S spike maintains native conformation.

With the aim of visualizing the conformational dynamics in real-time of SARS-CoV-2 S, we developed an smFRET imaging assay. We specifically sought to probe the movement of the RBD between the up and down positions. To this end, guided by the available structural data(*10*, *11*) (Fig. 1A), we inserted the 8-amino-acid A4 peptide into loops located between the β7-β8 strands in the NTD at position 161, and between helix α1 and strand β1 in the RBD at position 345 within the spike ectodomain (SΔTM, Fig. 1B). Fluorophores were then enzymatically attached to the A4 tag through incubation with AcpS(*27*). This approach was chosen because it was previously used for conformational dynamics studies of SARS-CoV-2 S, as well as the spike proteins from HIV-1 and Ebola(*18*, *28*, *29*). Our labeling strategy allowed us to track conformational changes in S that move the RBD between the up and down positions (Fig. 1C)(*18*). Structural analysis suggested a change of approximately 5 Å in the distance between the attachment sites of LD550 and LD650 fluorophores after the RBD transitions between the up and down conformations (Fig. 1A).

Homo-trimers of 161/345A4-tagged SΔTM, with either D614 or D614G, were validated through two different approaches: (1) evaluation of their binding to ACE2 and, (2) evaluation of their antigenic characteristics compared with unttaged SΔTM (Fig. S1A-B). We developed a fluorescence correlation spectroscopy (FCS) assay to evaluate ACE2 binding to A4-tagged SΔTM trimers in solution (Fig. 2A). For this assay, purified ACE2 (Fig. S1C) was conjugated to the Cy5 fluorophore (Fig. S1D). Cy5-ACE2 was incubated with varying concentrations of either tagged or untagged SΔTM and the timescale of diffusion was measured using FCS. The FCS data was fit to a model of two diffusing species(*30*) (Fig. 2B). Fitting led to determination of diffusion times for unbound ACE2 (τ_{free} = 0.48±0.02 ms), and ACE2 bound to SΔTM D614 ($\tau_{D614\text{-}bound}$ = 4.53±0.11 ms), and bound to the D614G variant ($\tau_{D614G\text{-}bound}$ = 4.32±0.15 ms). As expected, the diffusion times for the SΔTM-ACE2 complex were higher than for unbound ACE2, consistent with the formation of a larger complex with slower diffusion. Moreover, FCS experiments allowed us to calculate dissociation constants (K_D) for ACE2 binding to untagged and A4-tagged SΔTM proteins (Fig. 2C), which were approximately 12.4±2.7 nM and 8.3±1.2 nM, respectively, in rough agreement with values obtained through surface-based assays(*10*, *16*). The antigenicity of A4-tagged SΔTM homo-trimers was evaluated through an ELISA assay

112 described in Material and Methods, using the RBD-targeting antibodies MAb362 (both IgG_1 and
113 IgA_1)(*31*), REGN1098(*32*), S309(*33*) and CR3022(*34*); NTD-targeting antibody 4A8(*35*), as
114 well as the stalk-targeting antibodies 1A9(*36*) and 2G12(*37*) (Fig. S2A). A4-tagged SΔTM
115 homo-trimers maintained more than 50% of antibody binding compared to untagged SΔTM (Fig.
116 S2B), with MAb362-IgG1 and 4A8 showing no significant loss of binding. Taken together, these
117 results suggest that double 161/345 A4-labeled SΔTM trimers maintain native functionality
118 during ACE2 binding and near-native antigenic properties.

119

120 **ACE2 stabilizes the SARS-CoV-2 S RBD in the up conformation.**

121 To monitor the conformational dynamics of SΔTM D614 and D614G, we purified SΔTM hetero-
122 trimers (Fig. S1E-G), formed by co-transfection of 161/345A4-tagged and untagged SΔTM
123 plasmids at a 1:2 ratio (Material and Methods). This ensured that on average the SΔTM trimers
124 were comprised of one tagged protomer and two untagged protomers. The SΔTM hetero-trimers
125 were then labeled with equimolar concentrations of LD550 and LD650 fluorophores. The labeled
126 trimers were then incubated in the absence or presence of ACE2 before immobilization on a
127 quartz microscope slide and imaging with TIRF microscopy. smFRET trajectories acquired from
128 individual unbound SΔTM D614 molecules showed transitions between high (~0.65) and low
129 (~0.35) FRET states, suggestive of the down and up RBD positions, respectively (Fig. 3A).
130 Consistent with SΔTM D614 preferring the down conformation, analysis of the smFRET
131 trajectories with hidden Markov modeling (HMM) indicated 61.0±1.7% occupancy in the high-
132 FRET state and 39.0±1.7% occupancy in the low-FRET state. The same FRET states were
133 detected after incubation with ACE2, but the conformational equilibrium shifted to 36.8±2.1% in
134 the high-FRET state and 63.2±2.1% occupancy in the low-FRET state (Fig. 3B-C). HMM
135 analysis also indicated a reduction in the overall dynamics upon ACE2 binding, as indicated by
136 the transition density plots (TDPs; Fig. 3A-B), which display the relative frequencies of
137 transitions between the high- and low-FRET states. The rates of transition were determined
138 through maximum likelihood estimation. This analysis indicated that transition from the high- to
139 the low-FRET state occurred at k_{-1}=2.6±0.2 sec^{-1}, whereas the low- to high-FRET transition
140 occurred at k_1=3.8±0.2 sec^{-1}. ACE2 binding had minimal effect on the high- to low-FRET
141 transition (k_{-1}=2.2±0.2 sec^{-1}), but reduced the low- to high-FRET transition to k_1=1.3±0.1 sec^{-1}

142 (Fig. 3D). This analysis thus specified that the effect of ACE2 binding is to stabilize the low-
143 FRET state and reduce transitions to the high-FRET state. ACE2 binding does not significantly
144 affect the stability of the high-FRET state.

145 We next sought to determine the effect of the D614G mutation on the conformational dynamics
146 of SΔTM. We observed the same two FRET states for SΔTM D614G as for the ancestral D614
147 spike (Fig. 3E). However, the unbound SΔTM D614G displayed greater occupancy in the low-
148 FRET state (60.9±2.5%), and the overall level of dynamics was reduced as compared to D614
149 (Fig. 3E-G); the rate constants, k_{-1} and k_1, were reduced to 2.0±0.2 sec^{-1} and 1.6±0.2 sec^{-1},
150 respectively (Fig. 3H). ACE2 binding further increased the low-FRET occupancy to 74.5±2.2%
151 and reduced the overall level of dynamics shown in the TDPs (Fig. 3F). As for D614, ACE2
152 binding had minimal effect on the rate of transition from the high- to the low-FRET state (k_{-1}=2.0±0.4
153 sec^{-1}) but reduced the rate of transition from the low- to the high-FRET state to
154 k_1=0.7±0.1 sec^{-1} (Fig. 3H). Thus, consistent with structural studies(*16*, *19*), the D614G mutation
155 shifted the conformational equilibrium in favor of the up RBD conformation. Also, here again,
156 ACE2 binding stabilized the low-FRET up conformation without affecting the energetics of the
157 high-FRET down conformation.

158

159 **RBD-targeting antibodies promote the up RBD conformation of D614 spikes**

160 Numerous neutralizing monoclonal antibodies (mAbs) targeting SARS-CoV-2 S have been
161 identified(*38*). However, their mechanisms of action have only been partially described,
162 especially for antibodies that target epitopes outside of the RBD. We first sought to use our
163 smFRET imaging approach to explore the effect of RBD-directed antibodies on SΔTM dynamics
164 for both the D614 and D614G variants. We chose neutralizing RBD-directed mAbs from
165 different classified groups according to the epitope targeted(*39*): (1) MAb362 (isoforms IgG_1 and
166 IgA_1) that directly targets the ACE2-binding site in the RBM(*31*); (2) REGN10987, which binds
167 an epitope located on the side of the RBD, blocking ACE2 binding without directly interacting
168 with the RBM(*32*); and S309 and CR3022 that bind the RBD but do not compete with ACE2
169 binding(*33*, *34*). Imaging of SΔTM D614 pre-incubated with each of the above mAbs revealed a
170 predominant low-FRET state associated with the RBD in the up conformation (Fig. S3, left, and

171 Table S2). In all cases, the antibodies stabilized the low-FRET state as compared to the unbound
172 SΔTM, although none to the extent seen for ACE2 (Fig. 4A). As observed during ACE2 binding,
173 the antibodies generally induced a larger effect on the rate of transition from the low- to the high-
174 FRET state, with a minor effect on the high- to low-FRET transition (Fig. 4B). In contrast, none
175 of the antibodies stabilized the low-FRET state for SΔTM D614G to a significant extent (Figs.
176 4A, S3 and Table S3), suggesting that the effect of the D614G mutation is sufficient to enable
177 antibody binding without further conformational changes.

178

179 **NTD- and stalk-targeting mAbs allosterically modulate the RBD position**

180 Several mAbs have been identified that target epitopes outside of the RBD; some of which bind
181 the NTD and are potently neutralizing(*35*, *40–42*). We therefore explored the conformational
182 dynamics of both SΔTM D614 and D614G pre-treated with the NTD-targeting mAb 4A8(*35*),
183 and with the S2 stalk-directed mAbs 1A9(*36*) and 2G12(*37*). 4A8 treatment of SΔTM D614
184 stabilized the low-FRET state to a comparable extent as seen for the RBD-targeted mAbs (Figs.
185 4C, S3, and Table S2). The change in transition rates also followed a similar trend as seen for
186 RBD-targeted mAbs with the low- to high-FRET transition being reduced, with a minor effect on
187 the high- to low-FRET transition (Figs. 4D, S3, and Table S2). The stalk-directed mAbs 1A9 and
188 2G12 also stabilized the low-FRET state (Figs. 4C, S3, and Table S2), although kinetic analysis
189 revealed a modulation of the dynamics that was distinct from the S1-targeted mAbs. Here, the
190 rates of low- to high-FRET transition were reduced, while the rates of high- to low-FRET
191 transition were increased (Fig. 4D). For SΔTM D614G, 4A8 had only a minor effect on low-
192 FRET stability or kinetics, again suggesting that the mAb binds without affecting the
193 conformational equilibrium. However, the stalk-targeting 1A9 and 2G12 mAbs stabilized low
194 FRET and induced increases in the rates of transition out of high FRET (Fig. 4A, S3, and Table
195 S3). These data indicate that the S2 stalk-targeting mAbs studied here allosterically induce
196 transition of the RDB to the up conformation on both the D614 and D614G spikes. In contrast,
197 the RBD- and NTD-targeting antibodies studied here capture the up conformation without
198 actively inducing a conformational change.

199

200 **Stalk-targeting mAbs allosterically enhance ACE2 binding**

201 We next asked if stabilization of the RBD up conformation by NTD- and stalk-targeted mAbs
202 would increase ACE2 binding. We therefore applied our FCS assay for ACE2 binding after pre-
203 treating SΔTM D614 or D614G with mAbs (Material and Methods). MAb362IgA$_1$ and
204 REGN10987 mAbs were used as controls because of their documented ACE2-blocking
205 properties(*31*, *32*). Incubation of SΔTM D614 or D614G with MAb362IgA$_1$ or REGN10987
206 resulted in statistically significant reductions in ACE2 binding that are consistent with previous
207 reports(*31*, *32*) (Fig. 5). Overall, antibodies that stabilized the up conformation without blocking
208 the ACE2-binding site tended to promote ACE2 binding (Fig. 5A-B). Calculation of the
209 Spearman coefficient indicated a strong correlation (r_s = 0.7619) between ACE2 binding and
210 modulation of the SΔTM RBD conformational equilibrium across all the antibodies under
211 consideration (Fig. 5C). S309 and 4A8 provided a slight enhancement of ACE2 binding to
212 SΔTM D614, consistent with their impacts on RBD conformation. In contrast, S309 had no
213 significant effect on ACE2 binding to SΔTM D614G, and 4A8 had a slight inhibition of ACE2
214 binding, again consistent with their modulation of RBD conformation. Of particular note, the
215 stalk-targeting 1A9 and 2G12 antibodies induced the greatest enhancement of ACE2 binding to
216 SΔTM D614 and D614G, consistent with their allosteric modulation of RBD conformation.

217

218 **DISCUSSION**

219 Time-resolved analysis of viral spike protein conformation at single-molecule resolution
220 complements structural studies by specifying the effects of ligand binding on the energetics of
221 conformational dynamics. These analyses provide mechanistic insights unattainable from
222 structures and bulk functional data alone. Here, we have developed and applied an smFRET
223 imaging approach to monitor SARS-CoV-2 S conformational dynamics during engagement with
224 the ACE2 receptor and mAbs. Our analysis of S conformational dynamics shows that ACE2
225 stabilizes the RBD in the up conformation, which, in agreement with structural data, is a
226 conformation that pre-exists prior to ACE2 binding(*10*, *11*). Determination of the kinetics of
227 conformational changes through HMM indicate that ACE2 binding does not affect the rate of
228 transition to the up conformation. Instead, ACE2 captures the up conformation and reduces the

229 rate of transition to the down conformation. This analysis of S dynamics specifies that ACE2
230 binding to S does not induce a conformational change in S, but rather occurs through the capture
231 of a pre-existing conformation.

232 As ACE2 binding is an essential step during SARS-CoV-2 entry, our interpretation implicates
233 the intrinsic dynamics of S in controlling the rate or efficiency of membrane fusion during virus
234 entry. Current models of coronaviral membrane fusion depict the RBD-up conformation as an
235 intermediate state that is on-pathway to the post-fusion S conformation(*43*, *44*). Accordingly,
236 factors that stabilize the RBD-up conformation would likely increase the rate of membrane
237 fusion. Consistent with previous reports(*16*, *19*), our data demonstrate that the D614G mutation
238 stabilized the RBD-up conformation. Previous studies have shown that D614G does not increase
239 the rate of ACE2 binding to S(*16*, *19*), as might be expected for conformational capture binding
240 mechanism. This may indicate that further rearrangements in the RBD, perhaps localized in the
241 RBM, are necessary to fully engage ACE2 beyond transition to the up conformation. Analysis of
242 the dynamics of the unbound D614G variant showed an overall reduction in dynamics as
243 compared to D614, consistent with the increased stability of the S trimer with the D614G
244 mutation(*19*). Like ACE2 binding to the D614 spike, the predominant effect of the D614G
245 mutation was the reduction of the rate of transition to the down conformation, which accounts for
246 the increased occupancy in the up conformation. ACE2 binding to S D614G had an additive
247 effect on the RBD position, pushing the equilibrium further toward the up conformation than
248 either ACE2 binding or the D614G mutation did independently. Thus, the D614G mutation
249 permits further stabilization of an intermediate conformation captured by ACE2 binding. Residue
250 D614 is distal to the RBD and forms a salt bridge with K854 in the fusion-peptide proximal
251 region, which is lost with the D614G mutation(*17*, *19*, *45*). Such a long-range allosteric
252 connection between the receptor-binding domain and the region surrounding the fusion peptide
253 has been reported for influenza hemagglutinin(*46*), suggestive of a common mechanistic
254 connection between receptor binding and triggering movement of the fusion peptide among
255 class-I viral fusion proteins.

256 We find that mAbs that target S1 of the D614 spike, including the RBD and NTD, have a similar
257 impact on conformational dynamics as ACE2, with the predominant effect being the reduction in
258 the rate of transition to the down conformation. The overall minimal effect on the rate of

259 transition to the up conformation is again consistent with the capture of a pre-existing S
260 conformation. mAb S309 had a notably modest effect on the stability of the up conformation,
261 consistent with structural data demonstrating that it binds to the RBD in either the up or down
262 positions(*33*). Overall, RBD-and NTD-targeting mAbs had minimal effect on the conformation
263 of the D614G spike. The exception was mAb S309, which modestly destabilized the up
264 conformation, shifting the equilibrium to approximately that seen for the D614 spike bound to
265 S309. As S309 does not prevent ACE2 binding, its mechanism of broad neutralization remains
266 unclear(*33*, *47*). However, its modulation of the RBD position likely plays some role and may
267 impact downstream conformational changes related to membrane fusion.

268 Our kinetic analyses have shown that the S1-targeted ligands considered here capture the up
269 conformation, whereas S2-targeted mAbs considered here induce conformational changes in the
270 RBD. Cryo-electron tomography of SARS-CoV-2 virions has revealed the presence of three
271 flexible hinges within the S stalk: the hip, knee, and ankle. These hinges connect the head, and
272 the upper and lower legs of S and confer flexibility on the spikes(*48*, *49*). Our smFRET data
273 demonstrate that stalk-targeted mAbs 1A9 and 2G12 allosterically modulate the position of the
274 RBD, enhancing ACE2 binding. mAb 1A9, which neutralizes SARS-CoV, binds an epitope on S
275 in the upper leg of the stalk near the hip and upstream of the heptad repeat helix 2(*50*). High
276 sequence conservation in the 1A9 epitope suggests a similar binding site in SARS-CoV-2 S and
277 mode of action in preventing viral membrane fusion(*36*). The stalk epitope recognized by mAb
278 2G12, which does not neutralize SARS-CoV-2, is located near the hip and is comprised entirely
279 of glycans(*37*) (Fig. S2A). Taken together, our data on 1A9 and 2G12 implicate the hip hinge as
280 a critical center for allosteric control of the RBD position. Further support for the existence of
281 allosteric centers in S2 came from other smFRET analyses of mAb CV3-25(*51*), which binds an
282 epitope in the upper leg of the stalk near the knee(*23*). CV3-25 was also found to promote the
283 RBD-up conformation(*22*, *23*). Further studies are necessary to determine whether mAbs that
284 target the lower leg and ankle hinge also exert allosteric control of the RBD.

285 The use of therapeutic mAb cocktails is a promising strategy, which has been explored for the
286 treatment and prevention of Ebola virus disease(*52*). Similarly, enhancement of neutralization of
287 SARS-CoV-2 was observed with the simultaneous use of S309 and the S2E12(*53*, *54*), which
288 targets the RBM. This likely stems from the combined effect of S309 on S conformation and

289 blocking ACE2 binding by S2E12. Our results suggest similar synergy in neutralization might
290 come from the combination of 4A8 with RBM-directed mAbs. Indeed, human trials are
291 underway evaluating mAb cocktails for COVID-19 treatment. But none of these have considered
292 the simultaneous use of mAbs targeting the RBD and stalk of SARS-CoV-2 S(*25*, *38*). The
293 promotion of the RBD-up conformation, which exposes the ACE2-binding site, by NTD-directed
294 mAbs like 4A8, or stalk-directed mAbs like 1A9 and 2G12, presents a strategy for enhancement
295 of neutralization through combination therapies with RBM-directed mAbs. The results presented
296 here suggest the potential for synergistic inhibition of virus entry and increased potency through
297 the combination of mAbs that target diverse epitopes.

298

299 **MATERIALS AND METHODS**

300 **Cell culture**

301 ExpiCHO-S™ and Expi293F™ cell lines (Gibco™, Thermo Fisher Scientific, Waltham, MA,
302 USA) were cultured in ExpiCHO™ Expression and Expi293 Expression media (Gibco™, Thermo
303 Fisher Scientific, Waltham, MA, USA), respectively. Both cell lines were maintained at 37 ºC,
304 8% CO_2 with orbital shaking according to manufacturer instructions.

305

306 **Antibodies**

307 Monoclonal antibodies MAb362 isotypes IgG_1 and IgA_1 has been described before(*31*).
308 REGN10987, S309 and CR3022 antibodies heavy and light variable region sequences(*32*, *33*,
309 *55*) were synthesized and cloned into pcDNA3.1 vector (Invitrogen™, Thermo Fisher Scientific,
310 Waltham, MA, USA) in-frame with human IgG heavy or light chain Fc fragment. The
311 recombinant constructs of heavy and light chain were transfected at 1:1 ratio into Expi293F™
312 cells using the ExpiFectamine™ 293 Transfection Kit (Gibco™, Thermo Fisher Scientific,
313 Waltham, MA, USA). 4-5 days after transfection the antibodies were purified from the
314 supernatant by protein A affinity resin (ProSep®-vA ultra, Millipore®, Burlington, MA, USA)
315 and dialyzed into phosphate buffered saline pH 7.2 (PBS) overnight at 4 ºC. 2G12 monoclonal
316 antibody was expressed in ExpiCHO-S™ cells through co-transfection of plasmids encoding light

317 and IgG heavy chains(*56*), using the ExpiFectamine™ CHO transfection kit (Gibco™, Thermo
318 Fisher Scientific, Waltham, MA, USA) according to manufacturer instructions. The antibody
319 was purified from the cell culture supernatant 12 days post-transfection through protein G
320 affinity resin (Thermo Fisher Scientific, Waltham, MA, USA), and buffer exchanged and
321 concentrated in PBS using centrifugal concentrators (Sartorius AG, Göttingen, Germany;
322 Millipore®, Burlington, MA, USA). Monoclonal antibodies 4A8 and 1A9 were purchased from
323 BioVision (Milpitas, CA, USA) and GeneTex (Irvine, CA, USA), respectively. Anti-6x-His-tag
324 polyclonal antibody, and both HRP-conjugated anti-mouse IgG Fc and anti-human IgG Fc were
325 purchased from Invitrogen™ (Waltham, MA, USA). Both horseradish peroxidase (HRP)
326 conjugated anti-human kappa and anti-rabbit IgG were purchased from SouthernBiotech
327 (Birmingham, AL, USA) and Abcam (Cambridge, UK), respectively.

328

329 **Plasmids and site-directed mutagenesis**

330 The mammalian codon-optimized gene coding SARS-CoV-2 (Wuhan-Hu-1 strain, GenBank ID:
331 MN908947.3) glycoprotein ectodomain (SΔTM) (residues Q14–K1211) with SGAG substitution
332 at the furin cleavage site (R682 to R685), and proline substitutions at K986 and V987, was
333 synthesized by GenScript® (Piscataway, NJ, USA) and inserted into pcDNA3.1(-). A C-terminal
334 T4 fibritin foldon trimerization motif, a TEV protease cleavage site, and a His-tag were
335 synthesized downstream of the SARS-CoV-2 SΔTM (Fig. 1B). Insertion of A4 peptide
336 (DSLDMLEW) at amino acid position 161 in SARS-CoV-2 SΔTM was done through overlap-
337 extension PCR(*57*). Primers 2S-Age-I-F, 2S-161A4-2, 2S-161A4-3, and 2S-ApaI-R (Table S1)
338 were used in the PCR reactions to obtain a final product bearing the 161A4 insertion, which was
339 cloned into SΔTM using the AgeI and ApaI restriction sites. A similar strategy was performed
340 for the A4 insertion at position 345 of SΔTM using 2S-XhoI-F, 2S-345A4-2, 2S-345A4-3, and
341 2S-ApaI-R primers (Table S1) in the PCR reactions. The final PCR product bearing the 345A4
342 insertion was cloned into SΔTM using the XhoI and ApaI restriction sites. To generate the
343 161/345A4 double-tagged construct, the 345A4 insertion was subcloned into the 161A4
344 construct through XhoI and ApaI digestion. Mutagenic PCR to obtain the D614G amino acid
345 change into both untagged and 161/345A4-tagged SΔTM constructs was done using the primers
346 S2_D614_Q5-F and S2_D614_Q5-R (Table S1) and the Q5® Site-Directed Mutagenesis Kit

347 (NEB®, Ipswich, MA, USA) according to the manufacturer instructions. Insertions and site-
348 directed mutagenesis were confirmed through Sanger sequencing (GENEWIZ®, Cambridge,
349 MA, USA).

350

351 **Protein expression and purification**

352 Expression SΔTM trimers was performed by transfection of ExpiCHO-S™ cells with the
353 plasmids described above using the ExpiFectamine™ CHO transfection kit (Gibco™, Thermo
354 Fisher Scientific, Waltham, MA, USA) and according to manufacturer instructions. SΔTM
355 hetero-trimers for smFRET experiments were expressed by co-transfection with both the
356 untagged SΔTM (D614 or D614G) construct and the corresponding 161/345A4-tagged SΔTM
357 plasmid at a 2:1 molar ratio. Untagged SΔTM trimers or A4-tagged hetero-trimers were purified
358 from cell culture supernatants as follows. Supernatants containing soluble SΔTM trimers were
359 harvested nine days post-transfection and adjusted to 20 mM imidazole, 1 mM $NiSO_4$, and pH
360 8.0 before binding to the Ni-NTA resin. The resin was washed, and protein was eluted from the
361 column with 300 mM imidazole, 500 mM NaCl, 20 mM Tris-HCl pH 8.0, and 10% (v/v)
362 glycerol. Elution fractions containing SΔTM were pooled and concentrated by centrifugal
363 concentrators (Sartorius AG, Göttingen, Germany). The SΔTM protein was then further purified
364 by size exclusion chromatography on a Superdex 200 Increase 10/300 GL column (GE
365 Healthcare, Chicago, IL, USA) (Fig. S1). Double 161/345A4-tagged SΔTM homo-trimers for
366 functional assays were extracted from ExpiCHO-S™ cells at 6 days pot-transfection with a
367 Triton™ X-100 (Sigma-Aldrich®, St. Louis, MO, USA) based lysis buffer as described(*58*). The
368 tagged protein was then purified by affinity chromatography using Ni-NTA agarose beads
369 (Invitrogen™, Waltham, MA, USA) and size exclusion chromatography as described above.

370 A plasmid encoding soluble monomeric ACE2 with a C-terminal 6x-His tag was kindly provided
371 by Kuang Shen(*16*) and transfected into ExpiCHO-S™ cells as described above. Supernatant
372 containing ACE2 was harvested six days post-transfection, dialyzed at 4 ºC into 20 mM Tris-HCl
373 pH 8.0, 500 mM NaCl and 10% (v/v) glycerol buffer, using a 10 kDa MWCO dialysis membrane
374 (Spectrum® Repligen, Waltham, MA, USA). For ACE2 purification, the dialyzed supernatant
375 was supplemented with 20 mM imidazole pH 8.0 before purification as described above for

376 SΔTM. Purified protein concentrations were estimated by UV absorbance at 280 nm and
377 Bradford assay (Thermo Fisher Scientific, Waltham, MA, USA). SΔTM concentration was also
378 estimated by densitometric analysis of protein bands on immunoblots with the monoclonal
379 antibody 1A9 as described below, and using ImageJ software v1.52q (NIH, USA).

380

381 **PAGE and immunoblots**

382 Protein expression was evaluated by denaturing PAGE in 4-20% acrylamide (Bio-Rad, Hercules,
383 CA, USA) and either staining with Coomassie blue or with immunoblots performed as follows.
384 Protein gels were transferred into nitrocellulose membranes (Bio-Rad, Hercules, CA, USA)
385 according to the manufacturer instructions. After one hour of blocking with 5% (w/v) skim milk
386 in 0.1% (v/v) Tween™-20 (Fisher Scientific, Hampton, NH, USA) and PBS (PBS-T), membranes
387 were incubated by shaking overnight at 4 ºC with dilutions 1:2000 in blocking buffer of the
388 primary antibody. We used a rabbit anti-6X-His antibody (Invitrogen™, Waltham, MA, USA) to
389 detect histidine-tagged proteins or mouse 1A9 antibody (GeneTex, Irvine, CA, USA) for specific
390 detection of SARS-CoV-2 SΔTM. Membranes were washed three times with PBS-T and then
391 incubated with secondary HRP-conjugated anti-rabbit IgG (Abcam, Cambridge, UK) or anti-
392 mouse IgG (Invitrogen™, Waltham, MA, USA) antibodies diluted in 0.5% (w/v) skim milk/PBS-
393 T and incubated for one hour at room temperature. After three washes with PBS-T, membranes
394 were developed using SuperSignal™ West Pico PLUS Chemiluminescent Substrate (Thermo
395 Scientific™, Waltham, MA, USA) according to the manufacturer's instructions.

396

397 **ELISA assays**

398 96-well polystyrene plates (Thermo Scientific™, Waltham, MA, USA) were coated either with
399 200 ng of SARS-CoV-2 SΔTM proteins or bovine serum albumin (BSA, Thermo Scientific™,
400 Waltham, MA, USA) through incubation overnight at 4 ºC. Plates were washed three times with
401 PBS and blocked for one hour at room temperature with the immunoblot blocking buffer
402 described above. After three washes with PBS, plates were incubated with 600 nM of the
403 indicated antibodies diluted in PBS for two hours at room temperature. As secondary antibodies,
404 HRP-conjugated anti-human kappa antibody (SouthernBiotech, Birmingham, AL, USA) diluted

405 1:4000 in PBS was used in wells treated with MAb362, CR3022 and S309 antibodies, while
406 HRP-conjugated anti-human IgG Fc (Invitrogen™, Waltham, MA, USA) diluted 1:10,000 in PBS
407 was used in wells treated with REGN10987, 4A8 and 2G12 antibodies. A 1:5000 dilution of
408 HRP-conjugated anti-mouse IgG Fc antibody in PBS was used in 1A9 antibody-treated wells.
409 Plates were incubated with the secondary antibody dilutions for one hour at 37 ºC and developed
410 with 1-Step™ Ultra TBM-ELISA (Thermo Scientific™, Waltham, MA, USA) reagent according
411 to the manufacturer's instructions. The absorbances at 450 nm were measured using a Synergy
412 H1 microplate reader (BioTek® Winooski, VT). Absorbance values from non-specific binding to
413 BSA-coated wells were subtracted from the values obtained for SΔTM-coated wells. The
414 background-subtracted absorbance values were then normalized to the values obtained from
415 antibodies binding to untagged SΔTM.

416

417 **Fluorescent labeling of proteins**

418 Purified A4-tagged SΔTM hetero-trimers for smFRET imaging were prepared by overnight
419 incubation at room temperature with 5 μM each of coenzyme A (CoA)-conjugated LD550 and
420 LD650 fluorophores (Lumidyne Technologies, New York, NY, USA), 10 mM MgOAc, 50 mM
421 HEPES pH 7.5, and 5 μM Acyl carrier protein synthase (AcpS). Labeled protein was purified
422 away from unbound dye and AcpS by size exclusion chromatography as above described, and
423 elution fractions containing labeled SΔTM hetero-trimers were pooled and concentrated.
424 Aliquots were stored at -80 °C until use. Purified ACE2 was labeled with Cy5 conjugated to n-
425 hydroxysuccinimide ester (Cytiva, Marlborough, MA, USA) according to the manufacturer's
426 instructions. ACE2 was then purified away from unbound dye by Ni-NTA affinity
427 chromatography as described above, followed by buffer exchanged into PBS pH 7.4 using 10
428 kDa MWCO centrifuge concentrators (Millipore®, Burlington, MA, USA).

429 Purified LD550/LD650-labeled SΔTM spikes and Cy5-labeled ACE2 samples were analyzed by
430 denaturing PAGE and in-gel fluorescence was visualized using a Typhoon 9410 variable mode
431 imager (GE Amersham Biosciences, Amersham, UK) by laser excitation at 532 nm (emission
432 filter: 580 BP 30 Cy3) to detect LD550, or 633 nm (emission filter: 670 BP 30 Cy5) to detect
433 LD650 or Cy5 (Fig. S1).

434

435 **smFRET imaging**

436 Labeled SΔTM spikes (100-200 nM) were incubated in the absence or presence of unlabeled
437 ACE2 or the indicated antibody at a monomer:ACE2 or monomer:antibody ratio of 1:3 for 90
438 minutes at room temperature. The 6X-His tagged SΔTM was then immobilized on streptavidin-
439 coated quartz microscope slides by way of Ni-NTA-biotin (vendor) and imaged using wide-field
440 prism-based TIRF microscopy as described(*28*, *29*, *59*, *60*). Imaging was performed in the
441 continued presence of ligands at room temperature and smFRET data were collected using
442 Micromanager(*61*) v2.0 (micro-manager.org) at 25 frames/sec. All smFRET data were processed
443 and analyzed using the SPARTAN software (www.scottcblanchardlab.com/software) in Matlab
444 (Mathworks, Natick, MA, USA)(*62*). smFRET traces were identified according to following
445 criteria: mean fluorescence intensity from both donor and acceptor were greater than 50, duration
446 of smFRET trajectory exceeded 5 frames, correlation coefficient calculated from the donor and
447 acceptor fluorescence traces ranged between -1.1 to 0.5, and signal-to-noise ratio was greater
448 than 8. Traces that fulfilled these criteria were then verified manually. smFRET trajectories were
449 idealized to a 3-state hidden Markov model and the transition rates were optimized using the
450 maximum point likelihood algorithm(*63*), implemented in SPARTAN.

451

452 **FCS-based ACE2-binding assay**

453 ACE2 binding to the untagged and A4-tagged SΔTM spikes was evaluated by FCS as follows.
454 Several concentrations ranging from 0.1 to 200 nM SΔTM were incubated with 100 nM Cy5-
455 labeled ACE2 in PBS pH 7.4 for one hour at room temperature. Where indicated, 200 nM SΔTM
456 was incubated with 600 nM of the indicated antibody for one hour at room temperature, before
457 adding 100 nM Cy5-labeled ACE2. Non-specific antibody binding to Cy5-labeled ACE2 was
458 determined by incubation in the absence of SΔTM. Samples were then placed on No. 1.5
459 coverslips (ThorLabs, Newton, NJ) and mounted on a CorTector SX100 instrument (LightEdge
460 Technologies, Beijing, China) equipped with a 638-nm laser. 10-25 autocorrelation
461 measurements were made for 10 sec each at room temperature for each experimental condition.
462 To obtain the fractions of unbound and bound (*f*) ACE2 after incubation with SΔTM, normalized

463 autocorrelation curves were fit to a model of the diffusion of two species in a three-dimensional
464 Gaussian confocal volume(*64*, *65*),

465 $$G(\tau) = (1 - f) \cdot g_{unbound}(\tau) + f \cdot g_{bound}(\tau),$$

466 where

467 $$g_i(\tau) = \left(1 + \frac{\tau}{\tau_i}\right)^{-1} \left(1 + \frac{\tau}{s^2 \tau_i}\right)^{-1/2}$$

468 and τ_i is the diffusion time for bound or unbound ACE2 and s is the structure factor that
469 parameterizes the dimensions of the confocal volume. To determine $\tau_{unbound}$ FCS data was
470 obtained for ACE2 in the absence of SΔTM and fit to a model of a single diffusing species (f =
471 0). This value was then fixed during fitting of the FCS data obtained after incubation of ACE2
472 with SΔTM, so that only τ_{bound} and f were allowed to vary. ACE2 binding was expressed as the
473 average bound fraction (f) at each SΔTM concentration normalized either to the fraction bound at
474 the highest SΔTM concentration (Fig. 2C), or to the fraction bound in the absence of antibodies
475 (Fig. 5). All fitting was performed with a non-linear least-squares algorithm in MATLAB (The
476 MathWorks, Waltham, MA, USA). Dissociation constants (K_D) were determined using
477 GraphPad Prism version 9.2.0 (GraphPad Software, San Diego, CA, USA).

478

479 **Structural analysis**

480 Protein structures from RCSB PDB were visualized and analyzed using PyMOL™ software
481 version 2.0.7 (The PyMOL Molecular Graphic System, Schrödinger® Inc. New York, NY,
482 USA).

483

484 **Correlation and statistical analysis**

485 Data sets subjected to statistical analysis were first tested for normality using GraphPad Prism
486 version 9.2.0 (GraphPad Software, San Diego, CA, USA). Where indicated, statistical
487 significances were evaluated through either two-tailed parametric (unpaired t-test with Welch's
488 correction) or nonparametric (unpaired Mann-Whitney) tests. Both tests were performed with

95% confidence levels and P values <0.05 were considered significant. Significance values are indicated as *P<0.05, **P<0.01, ***P<0.001, ****P<0.0001. Two-tailed nonparametric Spearman test with 95% confidence was performed to evaluate the correlation level between the occupancy of SΔTM in the open conformation due to allosteric antibody binding and ACE2 binding (Figs. 4 and 5). The correlation level between the above variables was determined according to established criteria(*66*) regarding Spearman coefficients (r_s) rank values as follows: 0.00-0.10 = "negligible", 0.10-0.39 = "weak", 0.40-0.69 = "moderate", 0.70-0.89 = "strong", and 0.90-1.00 = "very strong" correlation.

REFERENCES

1. P. Zhou, X.-L. Yang, X.-G. Wang, B. Hu, L. Zhang, W. Zhang, H.-R. Si, Y. Zhu, B. Li, C.-L. Huang, H.-D. Chen, J. Chen, Y. Luo, H. Guo, R.-D. Jiang, M.-Q. Liu, Y. Chen, X.-R. Shen, X. Wang, X.-S. Zheng, K. Zhao, Q.-J. Chen, F. Deng, L.-L. Liu, B. Yan, F.-X. Zhan, Y.-Y. Wang, G.-F. Xiao, Z.-L. Shi, A pneumonia outbreak associated with a new coronavirus of probable bat origin. *Nature*. 579, 270–273 (2020).

2. Y.-J. Fan, K.-H. Chan, I. F.-N. Hung, Safety and Efficacy of COVID-19 Vaccines: A Systematic Review and Meta-Analysis of Different Vaccines at Phase 3. *Nato Adv Sci Inst Se*. 9, 989 (2021).

3. R. Rana, A. Tripathi, N. Kumar, N. K. Ganguly, A Comprehensive Overview on COVID-19: Future Perspectives. *Front Cell Infect Mi*. 11, 744903 (2021).

4. M. Letko, A. Marzi, V. Munster, Functional assessment of cell entry and receptor usage for SARS-CoV-2 and other lineage B betacoronaviruses. *Nat Microbiol*. 5, 562–569 (2020).

5. R. Yan, Y. Zhang, Y. Li, L. Xia, Y. Guo, Q. Zhou, Structural basis for the recognition of SARS-CoV-2 by full-length human ACE2. *Science*. 367, 1444–1448 (2020).

6. J. Lan, J. Ge, J. Yu, S. Shan, H. Zhou, S. Fan, Q. Zhang, X. Shi, Q. Wang, L. Zhang, X. Wang, Structure of the SARS-CoV-2 spike receptor-binding domain bound to the ACE2 receptor. *Nature*. 581, 215–220 (2020).

7. J. Shang, G. Ye, K. Shi, Y. Wan, C. Luo, H. Aihara, Q. Geng, A. Auerbach, F. Li, Structural basis of receptor recognition by SARS-CoV-2. *Nature*. 581, 221–224 (2020).

8. M. Hoffmann, H. Kleine-Weber, S. Schroeder, N. Krüger, T. Herrler, S. Erichsen, T. S. Schiergens, G. Herrler, N.-H. Wu, A. Nitsche, M. A. Müller, C. Drosten, S. Pöhlmann, SARS-

521 CoV-2 Cell Entry Depends on ACE2 and TMPRSS2 and Is Blocked by a Clinically Proven
522 Protease Inhibitor. *Cell*. 181, 271-280.e8 (2020).

523 9. Q. Wang, Y. Zhang, L. Wu, S. Niu, C. Song, Z. Zhang, G. Lu, C. Qiao, Y. Hu, K.-Y. Yuen, Q.
524 Wang, H. Zhou, J. Yan, J. Qi, Structural and Functional Basis of SARS-CoV-2 Entry by Using
525 Human ACE2. *Cell*. 181, 894-904.e9 (2020).

526 10. A. C. Walls, Y.-J. Park, M. A. Tortorici, A. Wall, A. T. McGuire, D. Veesler, Structure,
527 Function, and Antigenicity of the SARS-CoV-2 Spike Glycoprotein. *Cell*. 181, 281-292.e6
528 (2020).

529 11. D. Wrapp, N. Wang, K. S. Corbett, J. A. Goldsmith, C.-L. Hsieh, O. Abiona, B. S. Graham,
530 J. S. McLellan, Cryo-EM structure of the 2019-nCoV spike in the prefusion conformation.
531 *Science*. 367, 1260–1263 (2020).

532 12. A. C. Walls, M. A. Tortorici, J. Snijder, X. Xiong, B.-J. Bosch, F. A. Rey, D. Veesler,
533 Tectonic conformational changes of a coronavirus spike glycoprotein promote membrane fusion.
534 *P Natl Acad Sci Usa*. 114, 11157–11162 (2017).

535 13. M. A. Tortorici, D. Veesler, Structural insights into coronavirus entry. *Adv Virus Res*. 105,
536 93–116 (2019).

537 14. Y. Cai, J. Zhang, T. Xiao, H. Peng, S. M. Sterling, R. M. WalshJr., S. Rawson, S. Rits-
538 Volloch, B. Chen, Distinct conformational states of SARS-CoV-2 spike protein. *Science*. 369,
539 1586–1592 (2020).

540 15. J. Zhang, T. Xiao, Y. Cai, B. Chen, Structure of SARS-CoV-2 spike protein. *Curr Opin*
541 *Virol*. 50, 173–182 (2021).

542 16. L. Yurkovetskiy, X. Wang, K. E. Pascal, C. Tomkins-Tinch, T. P. Nyalile, Y. Wang, A.
543 Baum, W. E. Diehl, A. Dauphin, C. Carbone, K. Veinotte, S. B. Egri, S. F. Schaffner, J. E.
544 Lemieux, J. B. Munro, A. Rafique, A. Barve, P. C. Sabeti, C. A. Kyratsous, N. V. Dudkina, K.
545 Shen, J. Luban, Structural and Functional Analysis of the D614G SARS-CoV-2 Spike Protein
546 Variant. *Cell*. 183, 739-751.e8 (2020).

547 17. T. Zhou, Y. Tsybovsky, J. Gorman, M. Rapp, G. Cerutti, G.-Y. Chuang, P. S. Katsamba, J.
548 M. Sampson, A. Schön, J. Bimela, J. C. Boyington, A. Nazzari, A. S. Olia, W. Shi, M. Sastry, T.
549 Stephens, J. Stuckey, I.-T. Teng, P. Wang, S. Wang, B. Zhang, R. A. Friesner, D. D. Ho, J. R.
550 Mascola, L. Shapiro, P. D. Kwong, Cryo-EM Structures of SARS-CoV-2 Spike without and with
551 ACE2 Reveal a pH-Dependent Switch to Mediate Endosomal Positioning of Receptor-Binding
552 Domains. *Cell Host Microbe*. 28, 867-879.e5 (2020).

553 18. M. Lu, P. D. Uchil, W. Li, D. Zheng, D. S. Terry, J. Gorman, W. Shi, B. Zhang, T. Zhou, S.
554 Ding, R. Gasser, J. Prévost, G. Beaudoin-Bussières, S. P. Anand, A. Laumaea, J. R. Grover, L.
555 Liu, D. D. Ho, J. R. Mascola, A. Finzi, P. D. Kwong, S. C. Blanchard, W. Mothes, Real-Time

556 Conformational Dynamics of SARS-CoV-2 Spikes on Virus Particles. *Cell Host Microbe*. 28,
557 880-891.e8 (2020).

558 19. J. Zhang, Y. Cai, T. Xiao, J. Lu, H. Peng, S. M. Sterling, R. M. WalshJr., S. Rits-Volloch, H.
559 Zhu, A. N. Woosley, W. Yang, P. Sliz, B. Chen, Structural impact on SARS-CoV-2 spike
560 protein by D614G substitution. *Science*. 372, 525–530 (2021).

561 20. B. Korber, W. M. Fischer, S. Gnanakaran, H. Yoon, J. Theiler, W. Abfalterer, N. Hengartner,
562 E. E. Giorgi, T. Bhattacharya, B. Foley, K. M. Hastie, M. D. Parker, D. G. Partridge, C. M.
563 Evans, T. M. Freeman, T. I. de Silva, S. C.-19 G. Group, M. of S. C.-19 G. Group, A. Angyal, R.
564 L. Brown, L. Carrilero, L. R. Green, D. C. Groves, K. J. Johnson, A. J. Keeley, B. B. Lindsey, P.
565 J. Parsons, M. Raza, S. Rowland-Jones, N. Smith, R. M. Tucker, D. Wang, M. D. Wyles, C.
566 McDanal, L. G. Perez, H. Tang, A. Moon-Walker, S. P. Whelan, C. C. LaBranche, E. O.
567 Saphire, D. C. Montefiori, Tracking Changes in SARS-CoV-2 Spike: Evidence that D614G
568 Increases Infectivity of the COVID-19 Virus. *Cell*. 182, 812-827.e19 (2020).

569 21. D. Weissman, M.-G. Alameh, T. de Silva, P. Collini, H. Hornsby, R. Brown, C. C.
570 LaBranche, R. J. Edwards, L. Sutherland, S. Santra, K. Mansouri, S. Gobeil, C. McDanal, N.
571 Pardi, N. Hengartner, P. J. C. Lin, Y. Tam, P. A. Shaw, M. G. Lewis, C. Boesler, U. Şahin, P.
572 Acharya, B. F. Haynes, B. Korber, D. C. Montefiori, D614G Spike Mutation Increases SARS
573 CoV-2 Susceptibility to Neutralization. *Cell Host Microbe*. 29, 23-31.e4 (2020).

574 22. I. Ullah, J. Prévost, M. S. Ladinsky, H. Stone, M. Lu, S. P. Anand, G. Beaudoin-Bussières,
575 K. Symmes, M. Benlarbi, S. Ding, R. Gasser, C. Fink, Y. Chen, A. Tauzin, G. Goyette, C.
576 Bourassa, H. Medjahed, M. Mack, K. Chung, C. B. Wilen, G. A. Dekaban, J. D. Dikeakos, E. A.
577 Bruce, D. E. Kaufmann, L. Stamatatos, A. T. McGuire, J. Richard, M. Pazgier, P. J. Bjorkman,
578 W. Mothes, A. Finzi, P. Kumar, P. D. Uchil, Live imaging of SARS-CoV-2 infection in mice
579 reveals that neutralizing antibodies require Fc function for optimal efficacy. *Immunity*. 54, 2143-
580 2158.e15 (2021).

581 23. W. Li, Y. Chen, J. Prévost, I. Ullah, M. Lu, S. Y. Gong, A. Tauzin, R. Gasser, D. Vézina, S.
582 P. Anand, G. Goyette, D. Chaterjee, S. Ding, W. D. Tolbert, M. W. Grunst, Y. Bo, S. Zhang, J.
583 Richard, F. Zhou, R. K. Huang, L. Esser, A. Zeher, M. Côté, P. Kumar, J. Sodroski, D. Xia, P. D.
584 Uchil, M. Pazgier, A. Finzi, W. Mothes, *Biorxiv*, in press, doi:10.1101/2021.08.02.454546.

585 24. Y. Sun, M. Ho, Emerging antibody-based therapeutics against SARS-CoV-2 during the
586 global pandemic. *Antib Ther*. 3, tbaa025- (2020).

587 25. A. C. Hurt, A. K. Wheatley, Neutralizing Antibody Therapeutics for COVID-19. *Viruses*. 13,
588 628 (2021).

589 26. D. Corti, L. A. Purcell, G. Snell, D. Veesler, Tackling COVID-19 with neutralizing
590 monoclonal antibodies. *Cell*. 184, 3086–3108 (2021).

591 27. Z. Zhou, A. Koglin, Y. Wang, A. P. McMahon, C. T. Walsh, An Eight Residue Fragment of
592 an Acyl Carrier Protein Suffices for Post-Translational Introduction of Fluorescent Pantetheinyl
593 Arms in Protein Modification in vitro and in vivo. *J Am Chem Soc*. 130, 9925–9930 (2008).

594 28. N. Alsahafi, N. Bakouche, M. Kazemi, J. Richard, S. Ding, S. Bhattacharyya, D. Das, S. P.
595 Anand, J. Prévost, W. D. Tolbert, H. Lu, H. Medjahed, G. Gendron-Lepage, G. G. O. Delgado,
596 S. Kirk, B. Melillo, W. Mothes, J. Sodroski, A. B. Smith, D. E. Kaufmann, X. Wu, M. Pazgier, I.
597 Rouiller, A. Finzi, J. B. Munro, An Asymmetric Opening of HIV-1 Envelope Mediates
598 Antibody-Dependent Cellular Cytotoxicity. *Cell Host Microbe*. 25, 578-587.e5 (2019).

599 29. N. D. Durham, A. R. Howard, R. Govindan, F. Senjobe, J. M. Fels, W. E. Diehl, J. Luban, K.
600 Chandran, J. B. Munro, Real-Time Analysis of Individual Ebola Virus Glycoproteins Reveals
601 Pre-Fusion, Entry-Relevant Conformational Dynamics. *Viruses*. 12, 103 (2020).

602 30. J. Lakowicz, *Principles of Fluorescence Spectroscopy* (2006).

603 31. M. Ejemel, Q. Li, S. Hou, Z. A. Schiller, J. A. Tree, A. Wallace, A. Amcheslavsky, N. K.
604 Yilmaz, K. R. Buttigieg, M. J. Elmore, K. Godwin, N. Coombes, J. R. Toomey, R. Schneider, A.
605 S. Ramchetty, B. J. Close, D.-Y. Chen, H. L. Conway, M. Saeed, C. Ganesa, M. W. Carroll, L.
606 A. Cavacini, M. S. Klempner, C. A. Schiffer, Y. Wang, A cross-reactive human IgA monoclonal
607 antibody blocks SARS-CoV-2 spike-ACE2 interaction. *Nat Commun*. 11, 4198 (2020).

608 32. J. Hansen, A. Baum, K. E. Pascal, V. Russo, S. Giordano, E. Wloga, B. O. Fulton, Y. Yan,
609 K. Koon, K. Patel, K. M. Chung, A. Hermann, E. Ullman, J. Cruz, A. Rafique, T. Huang, J.
610 Fairhurst, C. Libertiny, M. Malbec, W. Lee, R. Welsh, G. Farr, S. Pennington, D. Deshpande, J.
611 Cheng, A. Watty, P. Bouffard, R. Babb, N. Levenkova, C. Chen, B. Zhang, A. R. Hernandez, K.
612 Saotome, Y. Zhou, M. Franklin, S. Sivapalasingam, D. C. Lye, S. Weston, J. Logue, R. Haupt,
613 M. Frieman, G. Chen, W. Olson, A. J. Murphy, N. Stahl, G. D. Yancopoulos, C. A. Kyratsous,
614 Studies in humanized mice and convalescent humans yield a SARS-CoV-2 antibody cocktail.
615 *Science*. 369, 1010–1014 (2020).

616 33. D. Pinto, Y.-J. Park, M. Beltramello, A. C. Walls, M. A. Tortorici, S. Bianchi, S. Jaconi, K.
617 Culap, F. Zatta, A. D. Marco, A. Peter, B. Guarino, R. Spreafico, E. Cameroni, J. B. Case, R. E.
618 Chen, C. Havenar-Daughton, G. Snell, A. Telenti, H. W. Virgin, A. Lanzavecchia, M. S.
619 Diamond, K. Fink, D. Veesler, D. Corti, Cross-neutralization of SARS-CoV-2 by a human
620 monoclonal SARS-CoV antibody. *Nature*. 583, 290–295 (2020).

621 34. M. Yuan, N. C. Wu, X. Zhu, C.-C. D. Lee, R. T. Y. So, H. Lv, C. K. P. Mok, I. A. Wilson, A
622 highly conserved cryptic epitope in the receptor binding domains of SARS-CoV-2 and SARS-
623 CoV. *Science*. 368, 630–633 (2020).

624 35. X. Chi, R. Yan, J. Zhang, G. Zhang, Y. Zhang, M. Hao, Z. Zhang, P. Fan, Y. Dong, Y. Yang,
625 Z. Chen, Y. Guo, J. Zhang, Y. Li, X. Song, Y. Chen, L. Xia, L. Fu, L. Hou, J. Xu, C. Yu, J. Li,
626 Q. Zhou, W. Chen, A neutralizing human antibody binds to the N-terminal domain of the Spike
627 protein of SARS-CoV-2. *Science*. 369, 650–655 (2020).

628 36. Z. Zheng, V. M. Monteil, S. Maurer-Stroh, C. W. Yew, C. Leong, N. K. Mohd-Ismail, S. C.
629 Arularasu, V. T. K. Chow, R. T. P. Lin, A. Mirazimi, W. Hong, Y.-J. Tan, Monoclonal
630 antibodies for the S2 subunit of spike of SARS-CoV-1 cross-react with the newly-emerged
631 SARS-CoV-2. *Eurosurveillance*. 25, 2000291 (2020).

632 37. W. B. Williams, R. R. Meyerhoff, R. J. Edwards, H. Li, K. Manne, N. I. Nicely, R.
633 Henderson, Y. Zhou, K. Janowska, K. Mansouri, S. Gobeil, T. Evangelous, B. Hora, M. Berry,
634 A. Y. Abuahmad, J. Sprenz, M. Deyton, V. Stalls, M. Kopp, A. L. Hsu, M. J. Borgnia, G. B. E.
635 Stewart-Jones, M. S. Lee, N. Bronkema, M. A. Moody, K. Wiehe, T. Bradley, S. M. Alam, R. J.
636 Parks, A. Foulger, T. Oguin, G. D. Sempowski, M. Bonsignori, C. C. LaBranche, D. C.
637 Montefiori, M. Seaman, S. Santra, J. Perfect, J. R. Francica, G. M. Lynn, B. Aussedat, W. E.
638 Walkowicz, R. Laga, G. Kelsoe, K. O. Saunders, D. Fera, P. D. Kwong, R. A. Seder, A.
639 Bartesaghi, G. M. Shaw, P. Acharya, B. F. Haynes, Fab-dimerized glycan-reactive antibodies are
640 a structural category of natural antibodies. *Cell*. 184, 2955-2972.e25 (2021).

641 38. D. Li, G. D. Sempowski, K. O. Saunders, P. Acharya, B. F. Haynes, SARS-CoV-2
642 Neutralizing Antibodies for COVID-19 Prevention and Treatment. *Annu Rev Med*. 73, 1–16
643 (2021).

644 39. E. Gavor, Y. K. Choong, S. Y. Er, H. Sivaraman, J. Sivaraman, Structural basis of SARS-
645 CoV-2 and SARS-CoV–antibody interactions. *Trends Immunol*. 41, 1006–1022 (2020).

646 40. N. Suryadevara, S. Shrihari, P. Gilchuk, L. A. VanBlargan, E. Binshtein, S. J. Zost, R. S.
647 Nargi, R. E. Sutton, E. S. Winkler, E. C. Chen, M. E. Fouch, E. Davidson, B. J. Doranz, R. E.
648 Chen, P.-Y. Shi, R. H. Carnahan, L. B. Thackray, M. S. Diamond, J. E. Crowe, Neutralizing and
649 protective human monoclonal antibodies recognizing the N-terminal domain of the SARS-CoV-2
650 spike protein. *Cell*. 184, 2316-2331.e15 (2021).

651 41. G. Cerutti, Y. Guo, T. Zhou, J. Gorman, M. Lee, M. Rapp, E. R. Reddem, J. Yu, F. Bahna, J.
652 Bimela, Y. Huang, P. S. Katsamba, L. Liu, M. S. Nair, R. Rawi, A. S. Olia, P. Wang, B. Zhang,
653 G.-Y. Chuang, D. D. Ho, Z. Sheng, P. D. Kwong, L. Shapiro, Potent SARS-CoV-2 neutralizing
654 antibodies directed against spike N-terminal domain target a single supersite. *Cell Host Microbe*.
655 29, 819-833.e7 (2021).

656 42. M. McCallum, A. D. Marco, F. A. Lempp, M. A. Tortorici, D. Pinto, A. C. Walls, M.
657 Beltramello, A. Chen, Z. Liu, F. Zatta, S. Zepeda, J. di Iulio, J. E. Bowen, M. Montiel-Ruiz, J.
658 Zhou, L. E. Rosen, S. Bianchi, B. Guarino, C. S. Fregni, R. Abdelnabi, S.-Y. C. Foo, P. W.
659 Rothlauf, L.-M. Bloyet, F. Benigni, E. Cameroni, J. Neyts, A. Riva, G. Snell, A. Telenti, S. P. J.
660 Whelan, H. W. Virgin, D. Corti, M. S. Pizzuto, D. Veesler, N-terminal domain antigenic
661 mapping reveals a site of vulnerability for SARS-CoV-2. *Cell*. 184, 2332-2347.e16 (2021).

662 43. J. Pallesen, N. Wang, K. S. Corbett, D. Wrapp, R. N. Kirchdoerfer, H. L. Turner, C. A.
663 Cottrell, M. M. Becker, L. Wang, W. Shi, W.-P. Kong, E. L. Andres, A. N. Kettenbach, M. R.
664 Denison, J. D. Chappell, B. S. Graham, A. B. Ward, J. S. McLellan, Immunogenicity and
665 structures of a rationally designed prefusion MERS-CoV spike antigen. *Proc National Acad Sci*.
666 114, E7348–E7357 (2017).

667 44. A. C. Walls, X. Xiong, Y.-J. Park, M. A. Tortorici, J. Snijder, J. Quispe, E. Cameroni, R.
668 Gopal, M. Dai, A. Lanzavecchia, M. Zambon, F. A. Rey, D. Corti, D. Veesler, Unexpected
669 Receptor Functional Mimicry Elucidates Activation of Coronavirus Fusion. *Cell*. 176, 1026-
670 1039.e15 (2019).

671 45. X. Xiong, K. Qu, K. A. Ciazynska, M. Hosmillo, A. P. Carter, S. Ebrahimi, Z. Ke, S. H. W.
672 Scheres, L. Bergamaschi, G. L. Grice, Y. Zhang, J. Bradley, P. A. Lyons, K. G. C. Smith, M.
673 Toshner, A. Elmer, C. Ribeiro, J. Kourampa, S. Jose, J. Kennet, J. Rowlands, A. Meadows, C.
674 O'Brien, R. Rastall, C. Crucusio, S. Hewitt, J. Price, J. Calder, L. Canna, A. Bucke, H.
675 Tordesillas, J. Harris, V. Ruffolo, J. Domingo, B. Graves, H. Butcher, D. Caputo, E. L. Gresley,
676 B. J. Dunmore, J. Martin, E. Legchenko, C. Treacy, C. Huang, J. Wood, R. Sutcliffe, J. Hodgson,
677 J. Shih, S. Graf, Z. Tong, F. Mescia, T. Tilly, C. O'Donnell, K. Hunter, L. Pointon, N. Pond, M.
678 Wylot, E. Jones, S. Fawke, B. Bullman, L. Bergamaschi, L. Turner, I. Jarvis, O. Omarjee, A. D.
679 Sa, J. Marsden, A. Betancourt, M. Perera, M. Epping, N. Richoz, G. Bower, R. Sharma, F. Nice,
680 O. Huhn, H. Stark, N. Walker, K. Stirrups, N. Ovington, E. Dewhust, E. Li, S. Papadia, J. A.
681 Nathan, S. Baker, L. C. James, H. E. Baxendale, I. Goodfellow, R. Doffinger, J. A. G. Briggs, A
682 thermostable, closed SARS-CoV-2 spike protein trimer. *Nat Struct Mol Biol*. 27, 934–941
683 (2020).

684 46. J. W. Yewdell, A. Taylor, A. Yellen, A. Caton, W. Gerhard, T. Bächi, Mutations in or near
685 the fusion peptide of the influenza virus hemagglutinin affect an antigenic site in the globular
686 region. *J Virol*. 67, 933–942 (1993).

687 47. M. McCallum, J. Bassi, A. D. Marco, A. Chen, A. C. Walls, J. D. Iulio, M. A. Tortorici, M.-
688 J. Navarro, C. Silacci-Fregni, C. Saliba, K. R. Sprouse, M. Agostini, D. Pinto, K. Culap, S.
689 Bianchi, S. Jaconi, E. Cameroni, J. E. Bowen, S. W. Tilles, M. S. Pizzuto, S. B. Guastalla, G.
690 Bona, A. F. Pellanda, C. Garzoni, W. C. V. Voorhis, L. E. Rosen, G. Snell, A. Telenti, H. W.
691 Virgin, L. Piccoli, D. Corti, D. Veesler, SARS-CoV-2 immune evasion by the B.1.427/B.1.429
692 variant of concern. *Science*. 373, 648–654 (2021).

693 48. B. Turoňová, M. Sikora, C. Schürmann, W. J. H. Hagen, S. Welsch, F. E. C. Blanc, S. von
694 Bülow, M. Gecht, K. Bagola, C. Hörner, G. van Zandbergen, J. Landry, N. T. D. de Azevedo, S.
695 Mosalaganti, A. Schwarz, R. Covino, M. D. Mühlebach, G. Hummer, J. K. Locker, M. Beck, In
696 situ structural analysis of SARS-CoV-2 spike reveals flexibility mediated by three hinges.
697 *Science*. 370, 203–208 (2020).

698 49. Z. Ke, J. Oton, K. Qu, M. Cortese, V. Zila, L. McKeane, T. Nakane, J. Zivanov, C. J.
699 Neufeldt, B. Cerikan, J. M. Lu, J. Peukes, X. Xiong, H.-G. Kräusslich, S. H. W. Scheres, R.
700 Bartenschlager, J. A. G. Briggs, Structures and distributions of SARS-CoV-2 spike proteins on
701 intact virions. *Nature*. 588, 498–502 (2020).

702 50. K.-M. Lip, S. Shen, X. Yang, C.-T. Keng, A. Zhang, H.-L. J. Oh, Z.-H. Li, L.-A. Hwang, C.-
703 F. Chou, B. C. Fielding, T. H. P. Tan, J. Mayrhofer, F. G. Falkner, J. Fu, S. G. Lim, W. Hong,
704 Y.-J. Tan, Monoclonal Antibodies Targeting the HR2 Domain and the Region Immediately
705 Upstream of the HR2 of the S Protein Neutralize In Vitro Infection of Severe Acute Respiratory
706 Syndrome Coronavirus. *J Virol*. 80, 941–950 (2006).

707 51. M. F. Jennewein, A. J. MacCamy, N. R. Akins, J. Feng, L. J. Homad, N. K. Hurlburt, E.
708 Seydoux, Y.-H. Wan, A. B. Stuart, V. V. Edara, K. Floyd, A. Vanderheiden, J. R. Mascola, N.
709 Doria-Rose, L. Wang, E. S. Yang, H. Y. Chu, J. L. Torres, G. Ozorowski, A. B. Ward, R. E.
710 Whaley, K. W. Cohen, M. Pancera, M. J. McElrath, J. A. Englund, A. Finzi, M. S. Suthar, A. T.
711 McGuire, L. Stamatatos, Isolation and characterization of cross-neutralizing coronavirus
712 antibodies from COVID-19+ subjects. *Cell Reports*. 36, 109353 (2021).

713 52. J. Misasi, N. J. Sullivan, Immunotherapeutic strategies to target vulnerabilities in the
714 Ebolavirus glycoprotein. *Immunity*. 54, 412–436 (2021).

715 53. M. A. Tortorici, M. Beltramello, F. A. Lempp, D. Pinto, H. V. Dang, L. E. Rosen, M.
716 McCallum, J. Bowen, A. Minola, S. Jaconi, F. Zatta, A. D. Marco, B. Guarino, S. Bianchi, E. J.
717 Lauron, H. Tucker, J. Zhou, A. Peter, C. Havenar-Daughton, J. A. Wojcechowskyj, J. B. Case,
718 R. E. Chen, H. Kaiser, M. Montiel-Ruiz, M. Meury, N. Czudnochowski, R. Spreafico, J. Dillen,
719 C. Ng, N. Sprugasci, K. Culap, F. Benigni, R. Abdelnabi, S.-Y. C. Foo, M. A. Schmid, E.
720 Cameroni, A. Riva, A. Gabrieli, M. Galli, M. S. Pizzuto, J. Neyts, M. S. Diamond, H. W. Virgin,
721 G. Snell, D. Corti, K. Fink, D. Veesler, Ultrapotent human antibodies protect against SARS-
722 CoV-2 challenge via multiple mechanisms. *Science*. 370, 950–957 (2020).

723 54. T. N. Starr, N. Czudnochowski, Z. Liu, F. Zatta, Y.-J. Park, A. Addetia, D. Pinto, M.
724 Beltramello, P. Hernandez, A. J. Greaney, R. Marzi, W. G. Glass, I. Zhang, A. S. Dingens, J. E.
725 Bowen, M. A. Tortorici, A. C. Walls, J. A. Wojcechowskyj, A. D. Marco, L. E. Rosen, J. Zhou,
726 M. Montiel-Ruiz, H. Kaiser, J. R. Dillen, H. Tucker, J. Bassi, C. Silacci-Fregni, M. P. Housley,
727 J. di Iulio, G. Lombardo, M. Agostini, N. Sprugasci, K. Culap, S. Jaconi, M. Meury, E. D. Jr, R.
728 Abdelnabi, S.-Y. C. Foo, E. Cameroni, S. Stumpf, T. I. Croll, J. C. Nix, C. Havenar-Daughton,
729 L. Piccoli, F. Benigni, J. Neyts, A. Telenti, F. A. Lempp, M. S. Pizzuto, J. D. Chodera, C. M.
730 Hebner, H. W. Virgin, S. P. J. Whelan, D. Veesler, D. Corti, J. D. Bloom, G. Snell, SARS-CoV-
731 2 RBD antibodies that maximize breadth and resistance to escape. *Nature*. 597, 97–102 (2021).

732 55. J. ter Meulen, E. N. van den Brink, L. L. M. Poon, W. E. Marissen, C. S. W. Leung, F. Cox,
733 C. Y. Cheung, A. Q. Bakker, J. A. Bogaards, E. van Deventer, W. Preiser, H. W. Doerr, V. T.
734 Chow, J. de Kruif, J. S. M. Peiris, J. Goudsmit, Human Monoclonal Antibody Combination
735 against SARS Coronavirus: Synergy and Coverage of Escape Mutants. *Plos Med*. 3, e237
736 (2006).

737 56. C. N. Scanlan, R. Pantophlet, M. R. Wormald, E. O. Saphire, R. Stanfield, I. A. Wilson, H.
738 Katinger, R. A. Dwek, P. M. Rudd, D. R. Burton, The Broadly Neutralizing Anti-Human
739 Immunodeficiency Virus Type 1 Antibody 2G12 Recognizes a Cluster of α1→2 Mannose
740 Residues on the Outer Face of gp120. *J Virol*. 76, 7306–7321 (2002).

741 57. K. L. Heckman, L. R. Pease, Gene splicing and mutagenesis by PCR-driven overlap
742 extension. *Nat Protoc*. 2, 924–932 (2007).

743 58. K. J. Petty, *Curr Protoc Protein Sci Éditor Board John E Coligan Et Al*, in press,
744 doi:10.1002/0471140864.ps0904s04.

745 59. D. K. Das, R. Govindan, I. Nikić-Spiegel, F. Krammer, E. A. Lemke, J. B. Munro, Direct
746 Visualization of the Conformational Dynamics of Single Influenza Hemagglutinin Trimers. *Cell*.
747 174, 926-937.e12 (2018).

748 60. D. K. Das, U. Bulow, W. E. Diehl, N. D. Durham, F. Senjobe, K. Chandran, J. Luban, J. B.
749 Munro, Conformational changes in the Ebola virus membrane fusion machine induced by pH,
750 Ca2+, and receptor binding. *Plos Biol*. 18, e3000626 (2020).

751 61. A. D. Edelstein, M. A. Tsuchida, N. Amodaj, H. Pinkard, R. D. Vale, N. Stuurman,
752 Advanced methods of microscope control using μManager software. *J Biological Methods*. 1,
753 e10 (2014).

754 62. M. F. Juette, D. S. Terry, M. R. Wasserman, R. B. Altman, Z. Zhou, H. Zhao, S. C.
755 Blanchard, Single-molecule imaging of non-equilibrium molecular ensembles on the millisecond
756 timescale. *Nat Methods*. 13, 341–344 (2016).

757 63. F. Qin, A. Auerbach, F. Sachs, A Direct Optimization Approach to Hidden Markov
758 Modeling for Single Channel Kinetics. *Biophys J*. 79, 1915–1927 (2000).

759 64. V. C. Ducas, E. Rhoades, Quantifying Interactions of β-Synuclein and γ-Synuclein with
760 Model Membranes. *J Mol Biol*. 423, 528–539 (2012).

761 65. J. Ries, P. Schwille, Fluorescence correlation spectroscopy. *Bioessays*. 34, 361–368 (2012).

762 66. P. Schober, C. Boer, L. A. Schwarte, Correlation Coefficients: Appropriate Use and
763 Interpretation. *Anesthesia Analgesia*. 126, 1763–1768 (2018).

764

765 **ACKNOWLEDGMENTS**

766 The authors thank Dr. Kuang Shen (UMass Chan Medical School) for providing the ACE2
767 expression plasmid, and Dr. Natasha Durham (UMass Chan Medical School) for critical
768 discussion and reading of the manuscript.

769

770 **FUNDING**

771 This work was supported by the UMass Chan Medical School COVID-19 Pandemic Relief Fund.

772

773 **AUTHOR CONTRIBUTIONS**

774 Project conceptualization, supervision, and manuscript review: JBM. Cloning, expression and
775 purification of RBD-directed mAbs: QL, ME, YW. Investigation, methodology, data analysis,
776 writing and editing original draft: MAD-S, JBM.

777

778 **COMPETING INTERESTS**

779 A patent application has been filed on May 5, 2020 on monoclonal antibodies targeting SARS-
780 CoV-2 (U.S. Patent and Trademark Office patent application no. 63/020,483; patent applicants:
781 Y.W., M.E., and Q.L., UMass Chan Medical School). The remaining authors declare no
782 competing interests.

783

784 **FIGURES**

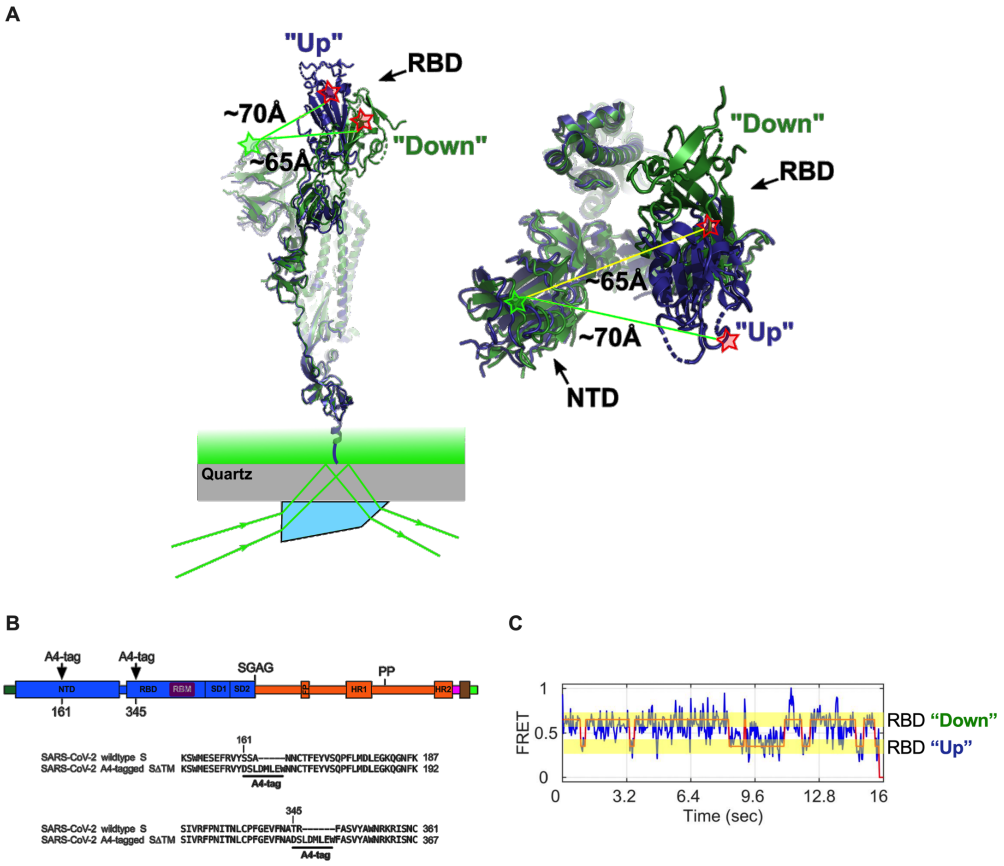

785

786 **Fig. 1. smFRET imaging the conformational dynamics of the SARS-CoV-2 S ectodomain.**
787 (**A**) (left) SARS-CoV-2 SΔTM containing a single fluorescently labelled A4-tagged protomer
788 within an otherwise untagged trimer was immobilized on a streptavidin-coated quartz
789 microscope slide by way of a C-terminal 8X His tag and biotin-NiNTA. For clarity, only a
790 monomer is depicted. Individual SΔTM trimers were visualized with prism-based TIRF
791 microscopy using a 532-nm laser. Overlay of two S protomers with RBD domains in the "up"
792 (blue) and "down" (green) conformations are shown with approximate positions of fluorophores
793 indicated by green (LD550) and red (LD650) stars. (right) Top view of the same S protomer
794 overlay. The approximate distances between the sites of labeling are shown. Structures adapted
795 from PDB 6VSB. (**B**) (top) Domain organization of the SARS-CoV-2 SΔTM construct used for
796 smFRET experiments, indicating the sites of A4 tag insertion. The S1 and S2 subunits are in blue
797 and orange, respectively. Additional domains and features are as follows, ordered from N- to C-
798 terminus: signal peptide, dark green; NTD, N-terminal domain; RBD and RBM, receptor binding

799 domain and motif (purple), respectively; SD1, subunit domain 1; SD2, subunit domain 2; SGAG,
800 furin cleavage site mutation; FP, fusion peptide; HR1 and HR2, heptad repeat 1 and 2,
801 respectively; PP, diproline mutations; T4 fibritin trimerization motif (foldon), magenta; TEV
802 protease cleavage site, brown; 8X-His tag, green; SGAG, sequence replacing furin-cleavage site.
803 (bottom) Amino acid sequence alignments indicating sites of A4-tag insertions in SΔTM. A4
804 peptide sequences (DSLDMLEW) are underlined. (**C**) Representative smFRET trajectory
805 acquired from an individual SΔTM trimer (blue). Idealization resulting from HMM analysis is
806 overlaid (red). High and low FRET states corresponding to the "down" and "up" positions of the
807 RBD, respectively, are indicated and highlighted in transparent yellow bars.
808

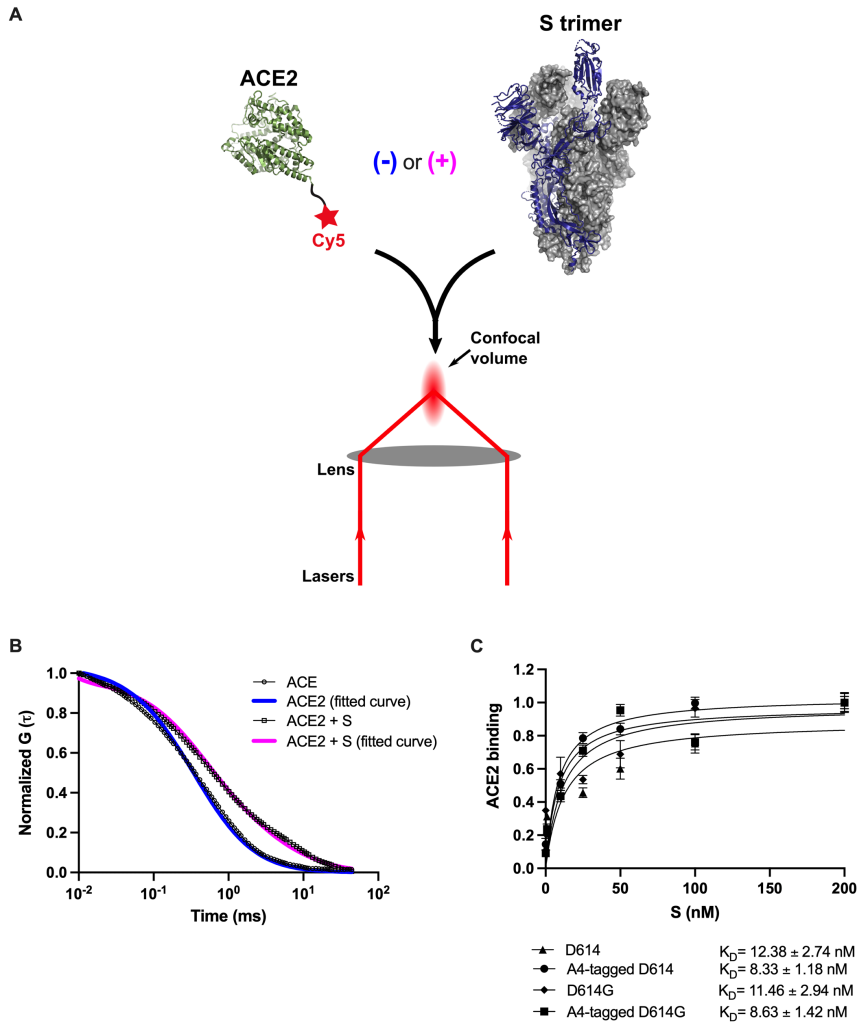

809

810 **Fig. 2. Verification of ACE2-binding to A4-tagged SΔTM trimers using FCS.** (**A**) Cy5-
811 labeled ACE2 was incubated in the absence or presence of untagged or A4-tagged SΔTM spikes.
812 The diffusion of Cy5-ACE2 was evaluated by FCS using a 647-nm laser as indicated at
813 Materials and Methods. (**B**) Representative normalized autocorrelation curves for Cy5-ACE2 in
814 the absence (circles) or presence (squares) of SΔTM, and the corresponding fits are shown in
815 blue or magenta, respectively. The shift in the autocorrelation to longer timescales seen in the
816 presence of SΔTM reflects the slower diffusion resulting from the larger size of the complex. (**C**)
817 Cy5-ACE2 (100 nM) was incubated with different concentrations of the indicated SΔTM spikes
818 and the resulting mixture was evaluated by FCS as described in Material and Methods.
819 Dissociation constants (K_D) determined from fitting the titration are indicated for the different

820 SΔTM constructs. Data are presented as the mean ± standard deviation from three independent
821 measurements.
822

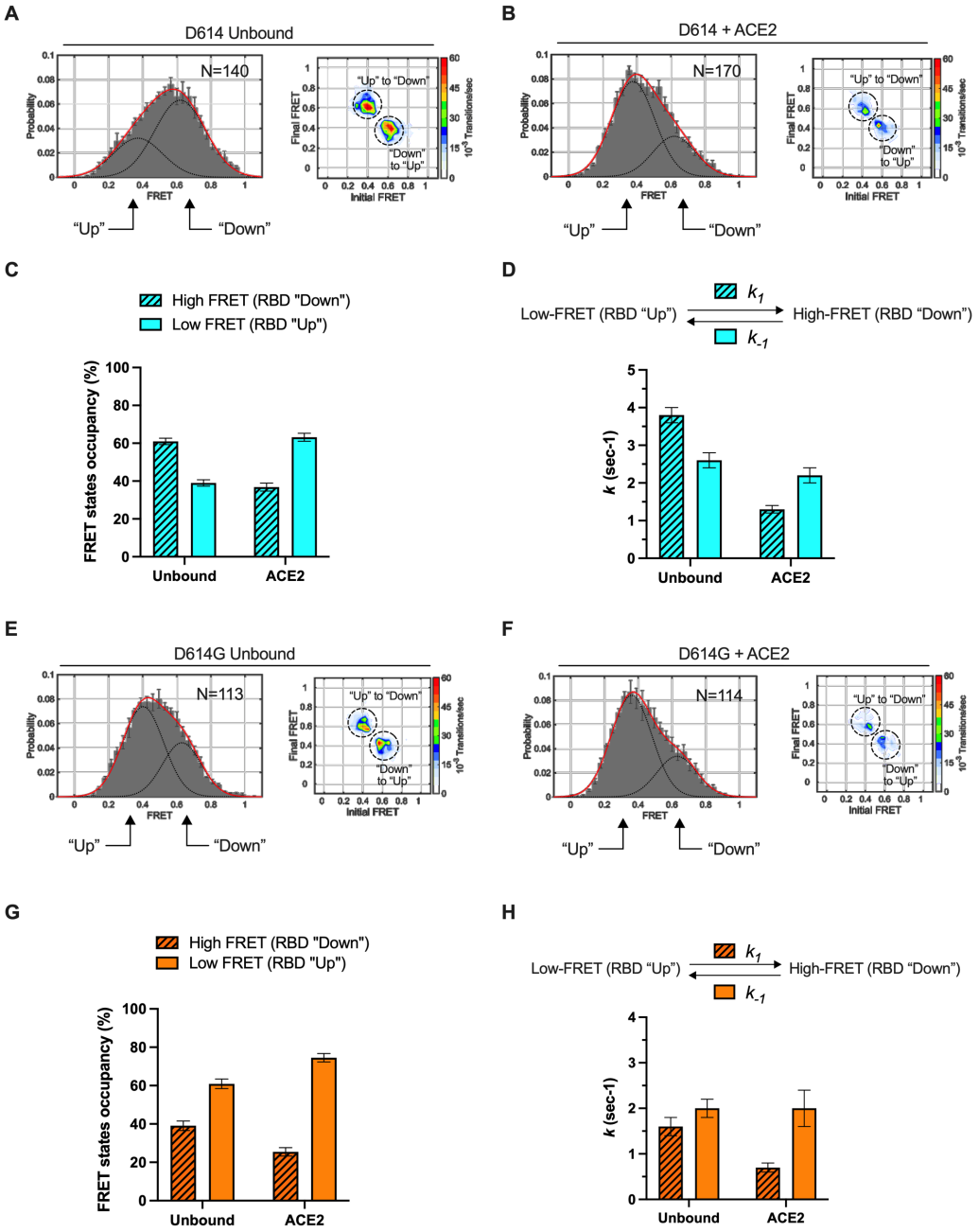

Fig. 3. ACE2-binding modulates the RBD conformation of SΔTM D614 and D614G. (**A**) (left) FRET histogram for unbound SΔTM D614 overlaid with the sum of two Gaussian distributions (sum, red; single distributions, grey) reflecting the results of HMM analysis. The Gaussian distributions are centered at 0.65 and 0.35 FRET, corresponding to the RBD-down and RBD-up conformations, respectively. FRET histograms are presented as the mean ± standard error determined from three independent populations of smFRET traces. The number of

830 smFRET traces compiled in the histogram is shown (N). (right) Transition density plot (TDP) for
831 unbound SΔTM D614 indicating the frequency of observed FRET transitions, as indicated,
832 determined through HMM analysis. (**B**) The same data for the ACE2-bound SΔTM D614 spike.
833 (**C**) Quantification of the high- and low-FRET state occupancies for unbound and ACE2-bound
834 SΔTM D614 determined from HMM analysis of the individual smFRET traces. Occupancies are
835 presented as the mean ± standard deviation across the population of traces. Numeric data are
836 shown in Table S2. (**D**) (top) Kinetic scheme defining the rates of transition between FRET
837 states. (bottom) Rates of transition for unbound and ACE2-bound SΔTM D614 determined from
838 HMM analysis of the individual smFRET traces. Rate constants are presented with error bars
839 estimated from 1000 bootstrap samples. Numeric data are shown in Table S2. (**E,F**) FRET
840 histogram and TDP for the unbound and ACE2-bound SΔTM D614G spike, displayed as in (A).
841 (**G,H**) FRET state occupancies and rates constants for the unbound and ACE2-bound SΔTM
842 D614G spike, displayed as in (C) and (D). Numeric data are shown in Table S3.
843

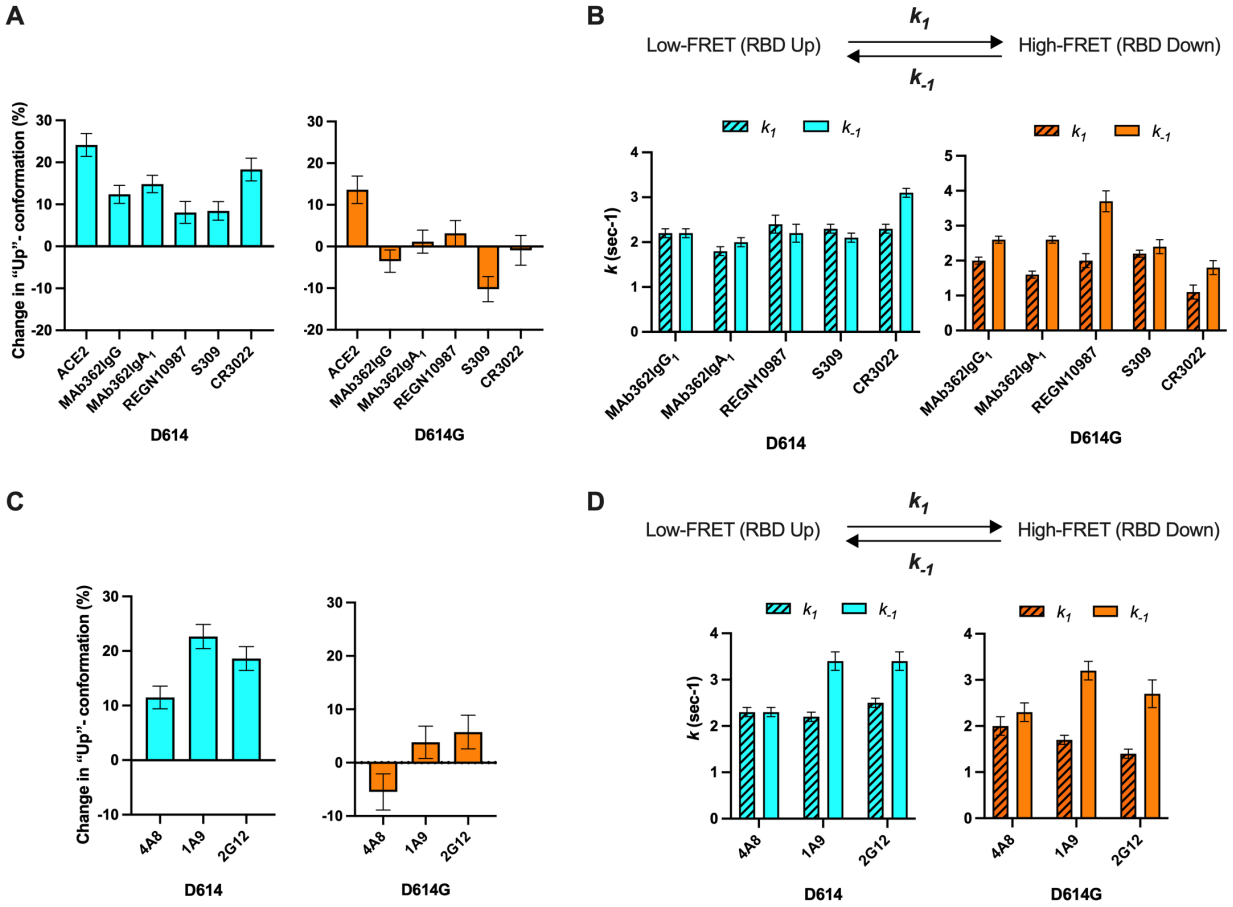

Fig. 4. Antibodies directly and allosterically modulate SΔTM RBD conformation. (**A**) The change in low-FRET occupancy (RBD-up conformation), calculated by subtracting the low-FRET occupancy for unbound SΔTM from that seen for SΔTM in the presence of the indicated ligand (ACE2 or RBD-targeted mAb). The changes in occupancy are shown for SΔTM D614 (cyan) and D614G (orange). (**B**) (top) Kinetic scheme defining the rates of transition between FRET states. (bottom) Rates of transition for SΔTM D614 (cyan) and D614G (orange) in the presence of RBD-targeted mAbs determined from HMM analysis of the individual smFRET traces. Rate constants are presented with error bars estimated from 1000 bootstrap samples. Numeric data are shown in Tables S2 and S3. (C) The change in low-FRET occupancy (RBD-up conformation) seen for SΔTM D614 (cyan) and D614G (orange) in the presence of NTD- (4A8) and stalk-targeted (1A9 and 2G12) mAbs. Data were determined as in (A). (**D**) Rates of

857 transition between FRET states for SΔTM D614 (cyan) and D614G (orange) in the presence of
858 NTD and stalk-targeted mAbs, presented as in (B). Numeric data are shown in Tables S2 and S3.
859

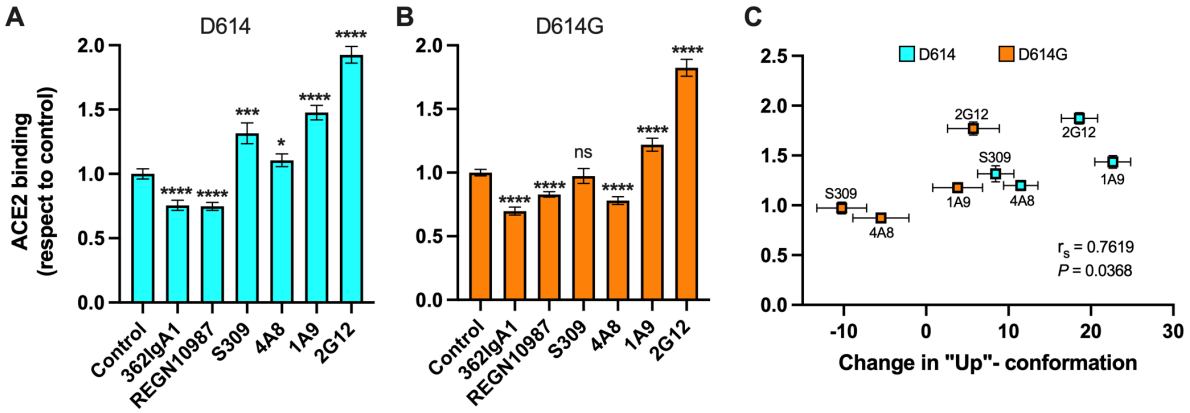

Fig. 5. Allosteric modulation of the RBD position promotes ACE2 binding. (**A**) Binding of ACE2 by (**A**) SΔTM D614 or (**B**) D614G spikes pre-incubated with the indicated mAbs was measured by FCS as described in Material and Methods. Data are presented as the average of two independent experiments, each consisting of forty 10-sec acquisitions. Statistical significance was evaluated through a two-tailed, unpaired Mann-Whitney test as indicated in Material and Methods. *P* values <0.05 were considered significant and significance values are indicated as **P*<0.05, ***P*<0.01, ****P*<0.001, *****P*<0.0001. (**C**) The change in the RBD-up conformation of SΔTM spikes pre-incubated with the indicated mAbs (Fig. 4A,C) exhibited a positive correlation with the binding of ACE2 determined through FCS. Statistical significance (*P*=0.0368) was found when Spearman test was performed with 95% of confidence (α=0.05).